A Mechanical Model of Early Somite Segmentation

Priyom Adhyapok[1], Agnieszka M Piatkowska[2],Sherry G Clendenon[1],

Claudio D Stern[2], James A Glazier[1], Julio M Belmonte[3*]

[1]Indiana University Bloomington, USA; [2]UCL, United Kingdom; [3]NC State University, USA

**corresponding author: jbelmon2@ncsu.edu*

Abstract:

The clock-and-wavefront model (CW) hypothesizes that the formation of body segments (somites) in vertebrate embryos results from the interplay of molecular oscillations with a wave traveling along the body axis. Our experiments, however, suggest that somites self-organize mechanically during a wave of epithelialization of the dorsal pre-somitic mesoderm that precedes somite segmentation in chicken embryos. Signs of somite formation first appear in the dorsal pre-somitic mesoderm, as a series of arched segments of epithelial monolayer separated by clefts. The clefts seem to correspond to the position of the eventual inter-somite boundaries. We develop a corresponding mechanical model of epithelial segmentation in early somitogenesis in which a wave of apical constriction leads to increasing tension and periodic failure of adhesion junctions within the dorsal epithelial layer of the PSM, forming clefts which determine the eventual somite boundaries. Computer simulations of this model can produce spatially periodic segments whose size depends on the speed of the contraction wave (W) and the rate of increase of apical contractility (Λ). We found that two values of the ratio Λ/W determines whether this mechanism produces spatially and temporally regular or irregular segments, and

whether segment sizes increases with the wave speed (scaling) as in the clock-and-wavefront model. Based on this, we discuss the limitations of a purely mechanical model of somite segmentation and the role that biomechanics play along with CW during somitogenesis.

Keywords: Somitogenesis, biomechanics, mesenchymal-to-epithelial transition

INTRODUCTION

Somitogenesis in vertebrate development sequentially and periodically creates metameric epithelial balls (somites) along the elongating embryo body from two rows of undifferentiated, loosely connected mesenchymal rods of cells called the pre-somitic mesoderm (PSM) while new PSM cells are continuously being deposited from the tail bud at the caudal (tail) end of the embryo (*Pourquié, (2001)*). At any given rostral-caudal position, a pair of nearly equal-sized somites form simultaneously on both sides of the neural tube, between the ectoderm and the endoderm. These transient structures are the precursors of vertebrae, ribs and many skeletal muscles, with many birth defects associated with a failure in one or more steps in this long developmental process (*Christ et al, (1995)*).

Somitogenesis is strikingly robust to perturbations (both spatial and temporal). Changes in the total number of embryonic cells or in the rate of new cell addition at the caudal end lead to compensating changes in the size and timing of somite formation so that the embryo eventually produces the same final number of somites as in normal

development (*Cooke, (1995)*). One way to achieve this conservation of final somite number is for the size of the somites to increase linearly (*scale*) with the speed of the caudal-moving position of the determination front or with the rate at which cells join the caudal end of the PSM.

Models seeking to explain somite formation include the ‘cell cycle model,’ which couples cells' somite fate to their cell-cycle phase (Stern et al (1988), Primmett et al (1988)) and reaction-diffusion models (*Meinhardt (1982), Cotterell et al (2015)*). Currently, the most widely accepted family of models employ a 'clock and wavefront' (CW) mechanism which combines caudally progressing waves of determination and differentiation with an intracellular oscillator which determines cell fate based on its phase at the moment of determination (*Cooke et al (1976))*. Following the identification of the first oscillating protein in the PSM (*Palmeirim et al (1997)*), many computer simulations, of varying complexity have implemented different CW models. Most CW models reproduce the experimentally observed scaling of somite size with clock period, wavefront speed and rate of elongation of the PSM (*Hester et al (2011), Tiedemann et al (2012), Baker et al (2006))*

Recent experiments have shown that somite-like structures can form without either a clock or a wavefront (*Dias et al (2014), Cotterell et al (2015)*). The ability of somites to form without clock or wavefront suggests that we should consider other mechanisms that could lead to spatially and temporally periodic sequential division of the PSM into regular segments. Recent experiments show that applied tension along the rostral-

caudal axis can induce the formation of intersomitic boundaries in locations not specified by clock-and-wavefront signaling (*Nelemans et al (2017)*), suggesting that mechanical mechanisms may be important in generating inter-somitic boundaries.

In 2009, Martins and colleagues imaged the morphology of cells during chicken somitogenesis *in vivo*, showing that cells elongate, crawl and align with each other as they form a somite (*Martins et al (2009)*). Cells in the PSM begin to change their behaviors gradually from mesenchymal to epithelial long before the formation of visible somites. Cells epithelialize gradually during somite formation, with epithelialization beginning long before segments separate from each other. Our recent experiments show that in addition to the classical rostral-caudal progression of epithelialization, epithelialization begins along the dorsal surface of the chicken PSM and propagates ventrally. As cells approach the time of the physical reorganization which generates somites they gradually increase the density of cell-cell adhesion molecules at the cell surface (*Duband et al (1987)*) and decrease their motility (*Bénazéraf et al (2010)*). When somites form, these gradual changes lead to a discontinuous change, somewhat like a jamming transition, where the tissue locally switches from extended and liquid-like to condensed and solid-like (in zebrafish) and the cells in each forming separate from those in the neighboring somite (*Mongera et al (2018)*).

Based on earlier observations of periodic (metameric) organization in the rostral-caudal direction before somite formation (which *Meier (1979)* and *Tam et al (1982)* called somitomeres) we performed Scanning Electron Microscopy (SEM) of chicken embryos

fixed at various stages of somitogenesis. These 3D SEMs consistently show that the dorsal monolayer of PSM cells begins to epithelialize and form a series of arched tissue three to four somite lengths caudal to the forming somite (Figure 1A). These cohorts are about the size of somites suggesting that they define the groups of cells that will form particular segments a few hours later.

These observations lead us to ask whether spatially and temporally periodic tissue segmentation and somite boundary positioning could result from a mechanical instability mechanism in the dorsal pre-somitic epithelium. We investigate a model in which a continuous caudally-travelling wave of apical constriction in the pre-somitic dorsal epithelium can lead to the sequential formation of periodic, spatially separated tissue segments. Our 2D simulation of a cross-section of the epithelial monolayer under this model can produce either constant-size segments or segments whose size increases (*scales*) with wave speed and inverse rate of increase of apical contractility. A roughly constant critical ratio of the wave speed to apical contractility build-up rate defines the boundary between these two domains. A second critical ratio also predicts when this mechanism produces spatially and temporally regular segments from irregular segments.

Early signs of boundary specification

To observe cell morphologies during somite formation, we fixed and sectioned sagittally chick embryos using a guillotine knife to produce planes of section almost perfectly

aligned to the embryonic midline along the entire body axis. We examined the embryos using Scanning Electron Microscopy (SEM). Preliminary observations (*Stern et al (2015)*) reveal that the dorsal region of the PSM starts to organize into a monolayer comprised of progressively elongated (columnar) cells as early as 4-5 somite-lengths caudal to the last-formed somite (S1).

Higher magnification SEM images of the PSM for a few somite lengths caudal to the forming somite reveal roughly periodic (in the rostral-caudal direction) clusters of cells of about 12 cells in length along the caudal-rostral axis(Figure 1A). Cells within these clusters are usually wedged shaped, with their apical (ventral facing) sides more constrited than their basal (dorsal facing) sides, which together gives the whole segment a dorsally arched aspect. The arched clusters are separated by what we refer to as clefts, or connecting regions, with cells that are either squeezed, apically separated, basaly constricted or non-elongated (arrowheads in Figure 1A). The distances between sequential clefts and between the first cleft and the S1 somite is regular and roughly corresponds to the caudal-rostral length of the future somites.

The observed position of the clefts between arched cell cluster closely corresponds to the posterior boundaries of the next somites to form (S-1,S-2 and S-3), suggesting that these structures arise from a pre-patterns mechanism of the future inter-somite boundary. At the same time, the overall convergence of the cells' apical sides between these clefts raise the possibility that apical constriction takes place in the pre-somitic dorsal epithelium as the PSM matures. Based on this we hypothesize a mechanical-

instability model for the segmentation of the dorsal pre-somitic epithelium. The model has two components: a caudally-travelling wave of apical contractility activation that leads to a gradual apical constriction of those cells (Figure 1C,D); and a maximum tension load between neighboring apical sides that determines the appearance of the clefts and segments the tissue (Figure 1E,F). The model assumes that the cells have an well-defined apical-basal polarity, and that cells are positionally constrained within a dorsally aligned monolayer, so that increased apical tension cannot be resolved by tissue curvature.

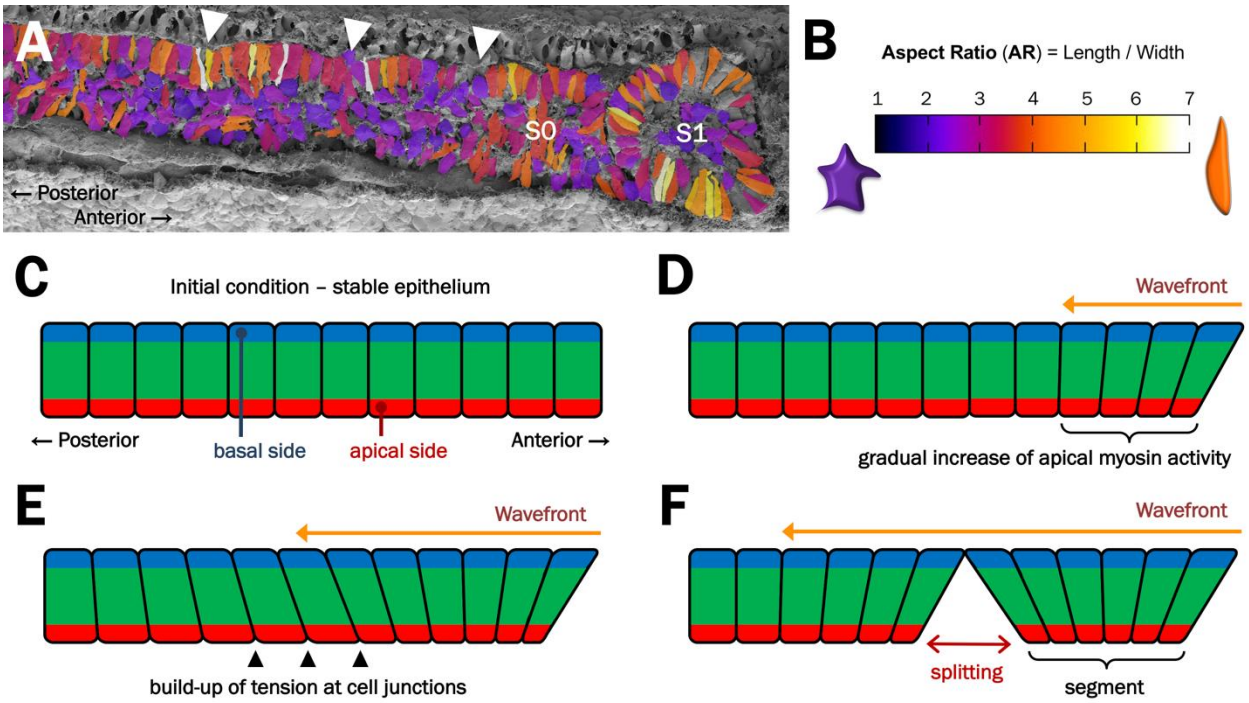

Figure 1 – Early signs of pre-somitic epithelium segmentation and conceptual model

(**A**) SEM images of para-sagitally sectioned chicken embryos shows the epithelialization of dorsal PSM cells about 5 somite-lengths caudal to the S1 somite. Cells are colored according to their aspect ratio, as shown in (**B**). White arrowheads show the positions of segmentation clefts. (**C**-**F**) Conceptual model of mechanical-instability mechanism of tissue segmentation. (**C**) Epithelialized cells, with defined apical (red) and basal (blue) sides form a rostral (right)-caudal (left) monolayer along the dorsal side of the PSM. (**D**) A caudal-moving wave of myosin activation (orange arrow) initiates apical constriction of the cells in the

monolayer. (**E**) As more cells begin to constrict apically, regions of high tension in the rostro-caudal direction develop within the tissue. (**F**) At some point the increasing tension causes the failure of the adhesion junctions between cells, leading to the appearance of a cleft/tear in the tissue (red double arrowed line) and the division of the initially continuous PSM into segmented pre-somitic epithelium.

A mechanical model of dorsal PSM pre-patterning for segmentation

Our model is focused on the cell behaviors of the pre-somitic dorsal epithelium. Based on the SEM observations, we start the simulations when the dorsal PSM cells have already started to form a monolayer, with defined apical and basal polarity, and an aspect ratio of 2:1 (Figure 2C). The basal sides of the cells face the ectoderm dorsally and their apical side faces the more ventral PSM cells. For simplicity we model the monolayer as single row of cells extended along the AP axis. The cells are aligned and flanked by each other in this monolayer. We propose that the cells are coupled together by labile adhesion along their entire surfaces and strong junctional adhesions located sub-apically (*Shirinifard et al (2012)*). The latter are or special importance as they also couple the apically localized actin-myosin cytoskeleton of neighboring cells.

As stated before, we hypothesize that the arched segments and clefts observed in this layer are due to the gradual activation of apical constriction along those cells. Myosin activity at the cells' apical side can generate contractile forces that reduce their apical surface area, give cells a wedge shape and bring together neighboring cells (Figure 1D) (*Baker et al (1967), Pilot et al (2005), Martin et al (2014), Sawyer et al (2010), Pearl et al (2017)*). Furthermore, if apical contractile forces exert too much load on junctional

adhesion sites, tissue tears appear, as observed in *Drosophila* embryos (*Martin et al (2010)*). Similar to a proposed 'determination front' at around the middle of the PSM (*Cooke et al (1976), Dubrulle et al (2001)*), we postulate a complementary, posteriorly travelling activation wave that induces apical constriction along the maturing PSM. As the wave passes, cells slowly increase their apical tension, eventually leading to the breaking of contacts between neighboring cells and the formation of a series of clefts that correspond to the future somite boundaries (Figure 1C-D). The speed at which this wave passes through the tissue (W) and the rate at which each pair of activated cell increases their apical contractility (Λ) are key parameters of our model that together determine the segmentation periodicity.

COMPUTATIONAL MODEL

Our model is implemented using the Cellular Potts (CPM), or Glazier-Graner-Hogeweg (GGH) model (*Graner et al (1992)*) and simulated with the open-source CompuCell3D software (*Swat et al (2012)*). In the CPM/GGH framework each cell, or cell region is spatially represented by a collection of pixels that forms a domain within a fixed grid (here, rectangular). Cell/domain properties such as size, mobility, adhesion preferences and distance constraints with other domains, are defined by a Hamiltonian, or energy cost-function:

(Eq. 1) $$H = H_0 + H_V + H_I + H_A + H_B,$$

where each term will be defined shortly.

The initial configuration of all cell/domains evolve in time by a series of random neighboring pixel copy attempts whose acceptance is governed by a Metropolis algorithm, with a number of pixel-flips equal to the grid size defining the time unit of the simulation, a Monte Carlo Step (MCS).

Similar to what has been done in previously models (*Belmonte et al (2016), Dias et al (2014)*), each cell is composed of 3 domains representing the apical, basal and core regions of an epithelial cell. The size of the domains is maintained by a volume constraint in the Hamiltonian:

(Eq. 2) $$H_{Volume} = H_V = \sum_{\sigma} \quad \lambda_V (V(\sigma) - V_T(\sigma))^2,$$

where the sum is over all domains (σ), $V(\sigma)$ is the current cell volume, $V_T(\sigma)$ is the cell target volume, and λ_V is a lagrangian multiplier setting the strength of the constraint.

The cell aspect ratio AR, defined as the ratio of apical/basal length to cell width, is maintained through the existence of spring-like distance constraints between the center of mass of the three domains belonging to the same cell:

(Eq. 3) $$H_{Internal\ Links} = H_I = \sum_{\sigma,\sigma'} \lambda_I (L(\sigma,\sigma') - L_{IT}(\sigma,\sigma'))^2,$$

where the sum is taken over all pairs of domains within the same cell, $L(\sigma,\sigma')$ is the current distance between the center of mass of the two domains, $L_{IT}(\sigma,\sigma')$ is the corresponding target distance, and λ_I is the strength of the constraint. To prevent cells from bending we set the target distance between apical and basal domains equal to the sum of the target distance between the core domain to the apical and basal domains.

Labile adhesion between cells is modeled with the standard Potts model Hamiltonian term:

(Eq. 4) $$H_{Labile\ adhesion} = H_0 = \sum_{i,j} J(\sigma_i,\sigma_j),$$

where the sum is taken over all fourth-order neighboring pairs of grid coordinates i and j, σ_i and σ_j are the cell domains at grid coordinates i and j, respectively, and J is the contact energy per unit area between those domains.

Apical constriction is a cell autonomous process that may lead to tissue-level events, such as invagination, through the coupling of the internal contractile activity of actin-myosin cytoskeleton of neighboring cells with their adhesion junctions. Since we are interested only on the tissue level effects of this process, we model junctional adhesion and apical constriction similar to (Eq. 3), with a distance constraint between neighboring apical domains:

(Eq. 5) $$H_{Apical\ links} = H_A = \sum_{\sigma,\sigma'} \lambda_A (L(\sigma,\sigma') - L_{AT})^2,,$$

where the sum is taken over all pairs of neighboring apical domains, $L(\sigma,\sigma')$ is the current distance between their center of mass, L_{AT} is the target distance, and $\lambda_A(\sigma,\sigma')$ is the time-varying strength of the constraint. The target distance between neighboring apical domains is constant throughout the simulations and set to a value much shorter than the width of the cells (3 pixels). Initially the constraint $\lambda_A(\sigma,\sigma')$, which we interpret here as the combined strength of apical cytoskeletal activity between cell pairs, is set very low ($\lambda_A = 20$), so that there is no effect on the tissue or individual cell shapes. A similar form ($H_{Basal\ links}$) is used for neighbouring basal domains with a fixed $\lambda_B = 100$. This is to help ensure the top part of the tissue stays together once the apical compartments have separated.

Above the basal side of cells, there is a collection of domains representing the ectoderm and fibronectin- and laminin-rich extracellular matrix that progressively forms a basal lamina (*Rifes et al (2007)*). These domains have a volume constraint and liable adhesion with the basal side of the epithelial cells that helps to maintain the alignment of the cells below them, while allowing some upward/downward movement of the cells. Below their apical sides, cells are adjacent to a loose mesenchyme which we choose to model as a single domain with no volume constraint and labile adhesion to the cells.

The epithelium is flanked anteriorly and posteriorly by relatively immotile cells, which are not allowed to change their shape or properties over time. Between them there are about 115 to 205 cells, depending on the conditions being tested in the simulations. Apart from the immotile cells that make the AP boundaries, all cells have identical properties and are allowed to change shape and properties during the course of the simulation.

Initially all cells are in an inactive state, without exerting significant forces on each other. We define a 'wave of constriction activation' which moves through the tissue from the anterior end at a fixed speed W(in units of cell/MCS), so that the next posterior cell is activated $1/W$MCS after the lastly activated cell. Apical constriction is implemented by a linear increase in the strength of apical cytoskeletal activity parameter λ_A between a pair of activated cells. This variable varies from a base value of 20 up to 600 at a specific build-up rate $\Lambda = d\lambda_A/dt$ (in units of 1/MCS). As a pair of cells increase their conjugated apical cytoskeletal activity parameter λ_A, the actual tension between their apical domains evolves in time, and is defined as:

(Eq. 6) $$T(\sigma,\sigma') = -2\,\lambda_A(L(\sigma,\sigma') - L_{AT})$$

When this tension value exceeds a maximum threshold $T_{break} = -7500$ the link between the apical domains of neighboring cells is broken, resulting in the appearance of a somitic cleft.

Variation in cell aspect ratios was implemented by adjusting the internal distance constraints between domains in Eq. 3. We also choose to keep the total sum of all domain target volumes constant and adjust the initial width and length of the cells to satisfy the internal distance constraints.

Standard Simulation Parameters

Our simulations have 4 key parameters, which we will vary systematically in this study:

1) *the wave speed* W, which travels from the anterior to the posterior end of the tissue and determines when cell pairs will start apical constriction;
2) *the rate of increase of apical contractility* (*build-up rate*) $\Lambda = d\lambda/dt$, which determines how fast neighboring cells strength of pull each other apical domains;
3) *the apical tension breaking threshold* T_{break}, which determines when the resulting tension (Eq. 6) will lead to the break of neighboring apical links (Eq. 5) and the split of the cell pairs; and
4) *the cell aspect ratio* AR, which defines how elongated the cells are at the beginning of the simulation.

The standard values of all 4 parameters can be found in (Table 1). A full list of all simulation parameters can be found in Supplementary Material.

Parameter	**Symbol**	**Base value (units)**
Wave speed	W	0.003 (cells/MCS)

Apical contractility build-up rate	Λ	0.05 (MCS^{-1})
Apical tension breaking threshold	T_{break}	-7500 (dimensionless)
Cell aspect ratio (height/width)	AR	2 (dimensionless)

Table 1 - Base values of the 4 key parameters of our model.

Metrics

To analyze the behavior of our model with respect to variation in key parameters we define and measure the following metrics:

1) *Average Segment Size* $< S >$: calculated by measuring the number of cells between two consecutive clefts in our simulations. We measure the sizes both during the course of the simulation - by taking into account the first occurence of a cleft located posteriorly to the posterior-most cleft - and at the end of the simulation in order to assess the presence of any splitting events.
2) *Average Distance Delay* $< D >$: defined as the distance between the wave position at the time of the last occurring cleft. This metric is measured during the time course of the simulation. This metric is calculated in units of the average segment size $< S >$ for the corresponding set of parameters.
3) *Average Segmentation Time* $< \tau >$: defined as the time (in MCS units) elapsed between the appearance of two consecutive clefts.

To avoid boundary effects, all parameters are measured after the appearance of the first segmentation cleft and before a distance of $3 < S >$ from the last formed cleft to the posterior boundary.

RESULTS

Tension profiles as a function of number of cells and constriction strength

We first test our model by creating small epithelial monolayers composed of 4 to 16 cells of fixed aspect ratio $AR = 2$ (Figure 2A). The strength of apical contractility of all cell pairs was increased simultaneously at a fixed build up rate of $\Lambda = 0.05$, from $\lambda_A = 0$ up to a maximum value of $\lambda_A = 600$, without enforcing breakage of apical links. We then observe the shape of the tissue and the average cell pair tension (Eq. 6) over 20,000 MCS after λ_A has reached the maximum value. As the chain increases in size, cell pairs in the middle of the segment are under higher tension compared to cell pairs near the periphery (Figure 2B,C). This forms the premise of our model - as the tissue becomes larger, more tension is accumulated by the cell pairs which, in the presence of a maximum tension load, predisposes the tissue to regular segmentation.

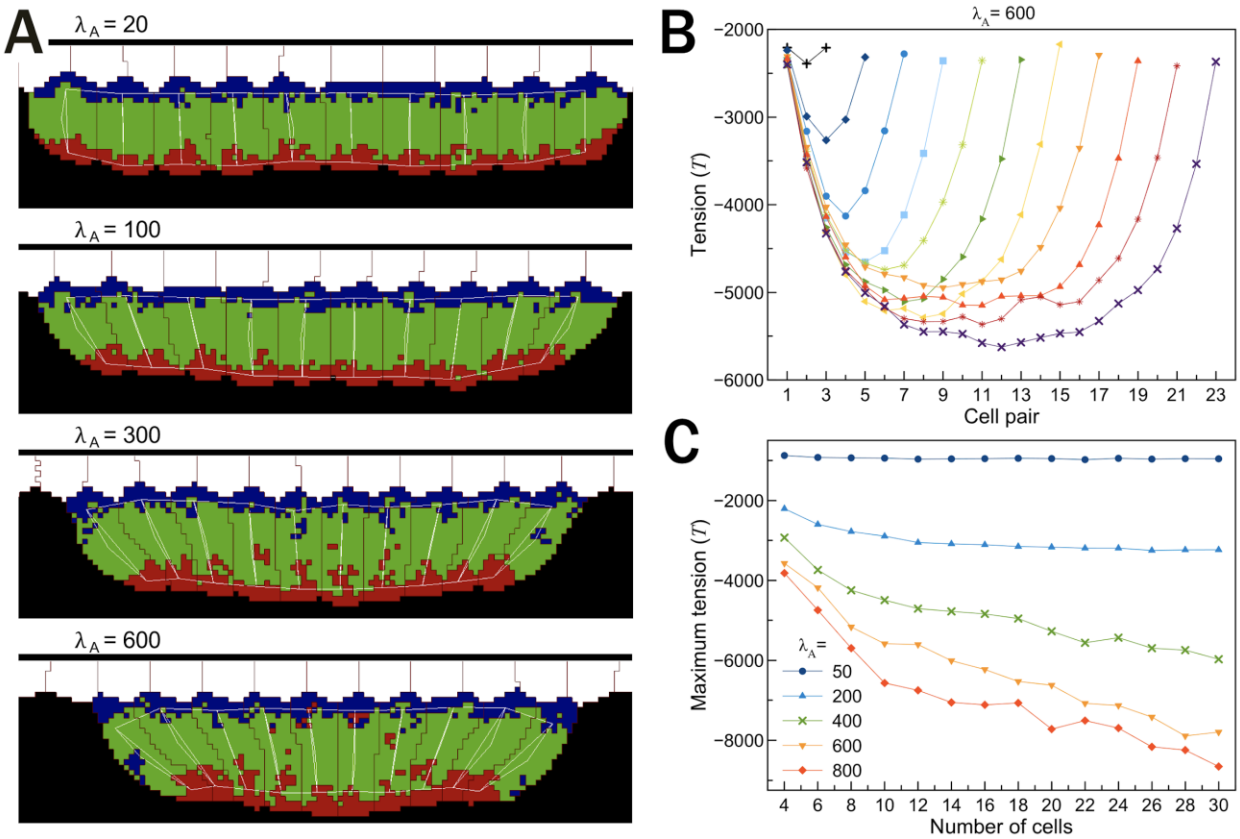

Figure 2 - Tissue tension distribution as a function of the strength of apical contractility

(**A**) Snapshots of 4 simulations of 10 cells with different levels of apical contractility strength. The higher the levels of λ_A the more constricted the tissue becomes. (White - ectodermal tissue; black - non-modeled PSM; cells domain colors as in Figure 1C-F; vertical white lines - internal distance constraints between cell domains (Eq. 3); horizontal white lines - distant constraints between domains of neighboring cells (Eq. 5)). (**B**) Plot of average apical tension (Eq. 6) between cell pairs at the end of multiple simulations with different number of cells (from 4 to 24). In all these simulations λ_A is set to 600. (**C**) Plot of maximum cell pair tension versus the number of cells in the tissue for different values of λ_A.

Gradual and sequential activation of apical contractility leads to tissue segmentation

Next we investigated whether sequential activation of apical constriction can slice a tissue to generate regularly sized segments. From now on, all simulations have a large number of cells and a posteriorly travelling wave of activation sequentially initiates a gradual and linear increase of the strength of apical contractility of cell pairs. The wave speed W and build-up rate of apical contractility Λ will be varied systematically around their base values (see Table1). In addition, apical cell pairs will have a maximum tension load T_{break}, after which their links break and a tear may appear between the apical region of those cells.

Figure 3A shows a time series of a zoomed-in section of a simulation with 115 cells where 4 tissue segments form. With the exception of the first and last two segments (due to boundary conditions), all segments are of similar size ($< S >= 11.36 \ +/- \ 1.45$) and clefts form at similar time intervals ($< \tau >= 3442.37 \ +/- \ 587.87$) for our standard set of parameter values (see Table1). We also looked at the evolution of the tension profile for 3 sequential segments. As the wave passes, the tension between cell pairs gradually increases, with the anterior-most pair with the higher tension (Figure 3B and green lines in Figure 3C). After the formation of the anterior cleft/boundary the pattern is inverted, with the anterior-most cell pairs now more relaxed and the posterior most pairs now under higher tension (compare green and blue lines in Figure 3C). Formation of the posterior-most cleft/boundary relaxes the tension of these pairs and the segment

tension profile has now a symmetrically convex shape with an average lower tension compared with the intermediate steps (black lines in Figure 3C). The same process repeats itself in the formation of the subsequent segments.

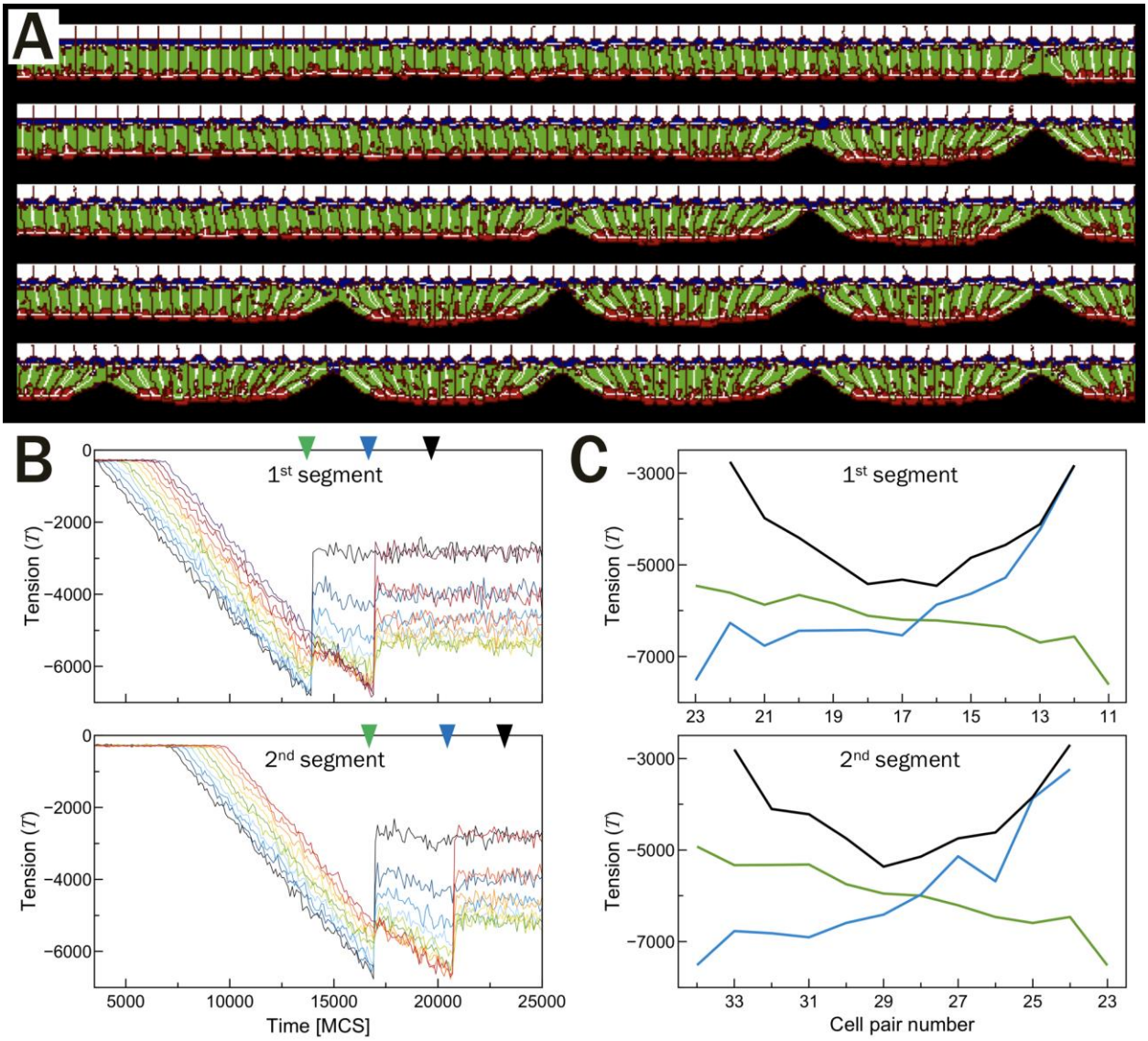

Figure 3 - Tissue segmentation from wave of apical constriction

(**A**) Time-series of a simulation showing the sequential segmentation of a tissue due to a linear increase of apical cytoskeletal activity as cells are progressively activated from anterior (right) to posterior (left). Colors as in Figure 3A. Snapshots taken at the approximate moment the clefts are formed (17000, 21000, 24000, 28000 and 31000 MCS). (**B**) Time evolution of cell pair tensions for cells in the regions of 2 consecutive segments. Cells are counted from the anterior position (right). (**C**) Tension profiles for the 2

tissue segments shown in (**B**). Each line corresponds to the same-color arrowheads in (**B**) and indicate three different events - formation of the anterior segment boundary (green), formation of posterior segment boundary (blue), and some time after the posterior event occurs (black).

Segment size scaling with wave speed and rate of apical constriction

One of the attractive features of the clock and wavefront model, even before the identification of the first oscillating gene in the PSM, was its ability to explain how somite size can adjust to variations of embryo size: a faster clock would produce smaller somites, while a faster wavefront would generate larger somites. We now investigate if our mechanical model of segmentation has the same scaling features: does a faster wave of activation (W) lead to larger segments? And how does this scaling change with the associated build-up rate of apical contractility (Λ)? In the results that follow we systematically varied both parameters and all data points have been averaged over 5 simulations with 115 to 205 cells.

We first fixed the build-up rate of apical contractility Λ and varied the wave speed W. We observe two regimes of the average segment size $< S >$ with respect to the wave speed. For wave speeds below a critical value ($< W^*$) average segment size $< S^* >$ was constant, but increases as a power law with exponents close to ¼ for faster wave speeds ($> W^*$) (Figure 4A). The critical value of the wave speed $W^*$for the change to the scaling regime, as well as the average segment sizes $< S^* >$ before scaling depends on the value of the build-up rate Λ (Figure 4B). These results suggest that the discrete spatial compartmentalization of the tissue in cell units poses a lower limit on

segment size as a function of Λ (Figure 4B). In fact, our simulations in absence of a wave already indicates that the maximum tension a cell pair can reach depends on the number of cells within a forming segment (Figure 2B), so for slow waves we expect the cleft always appearing at the same size intervals.

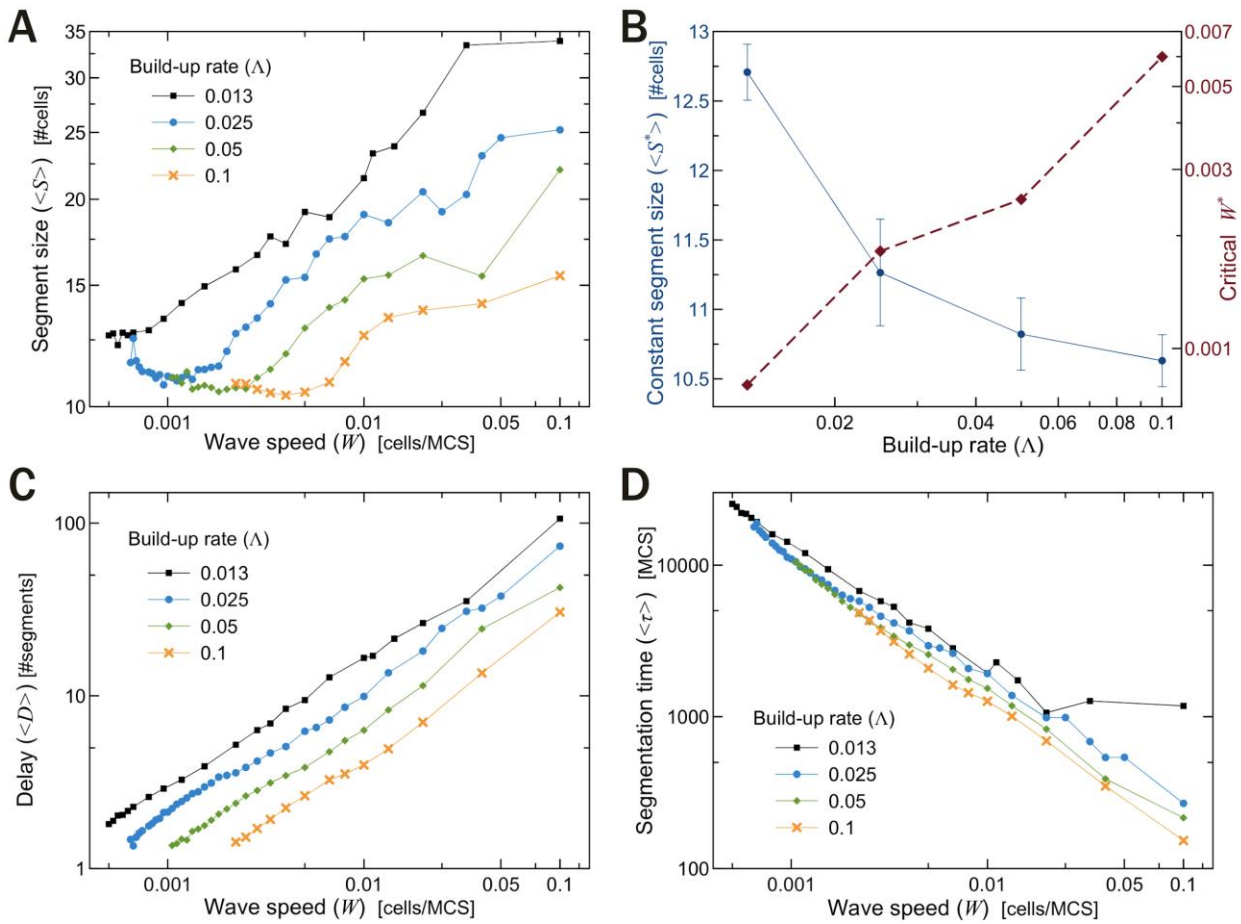

Figure 4 - Segmentation as a function of wave speed
(**A**) Average segment size $< S >$as a function of wave speed W. For short wave speeds segments are of roughly constant size, but scale as a power law afterwards. (**B**) Constant segment sizes $< S^* >$ (blue solid line) and critical wave speeds W^* (red dashed line) as functions of Λ. (**C**) Spatial delay between activation and boundary formation $< D >$ scales linearly with W. (**D**) Average segmentation time $< \tau >$ decreases as a power law with $W^{-0.80\pm0.008}$. (**A**,**C**,**D**) Each line shows a similar behavior for different base values of the build-up rate of apical contractility (Λ).

The average distance between apical constriction activation and boundary formation $< D >$ showed a less surprising behavior with an approximate linear scaling with wave speed (Figure 4C): the faster the wave, the larger the distance between the wavefront and the boundaries. Changes in the base value of Λ only shifted the curves, with lower build-up rates increasing the spatial delay between activation and boundary formation. The average time interval between successive boundary formation $< \tau >$, however, was insensitive to the build-up rate of apical contractility Λ. This output only depends on W, with faster wave speeds decreasing the segmentation time as a power law with exponent -0.80 ± 0.008.

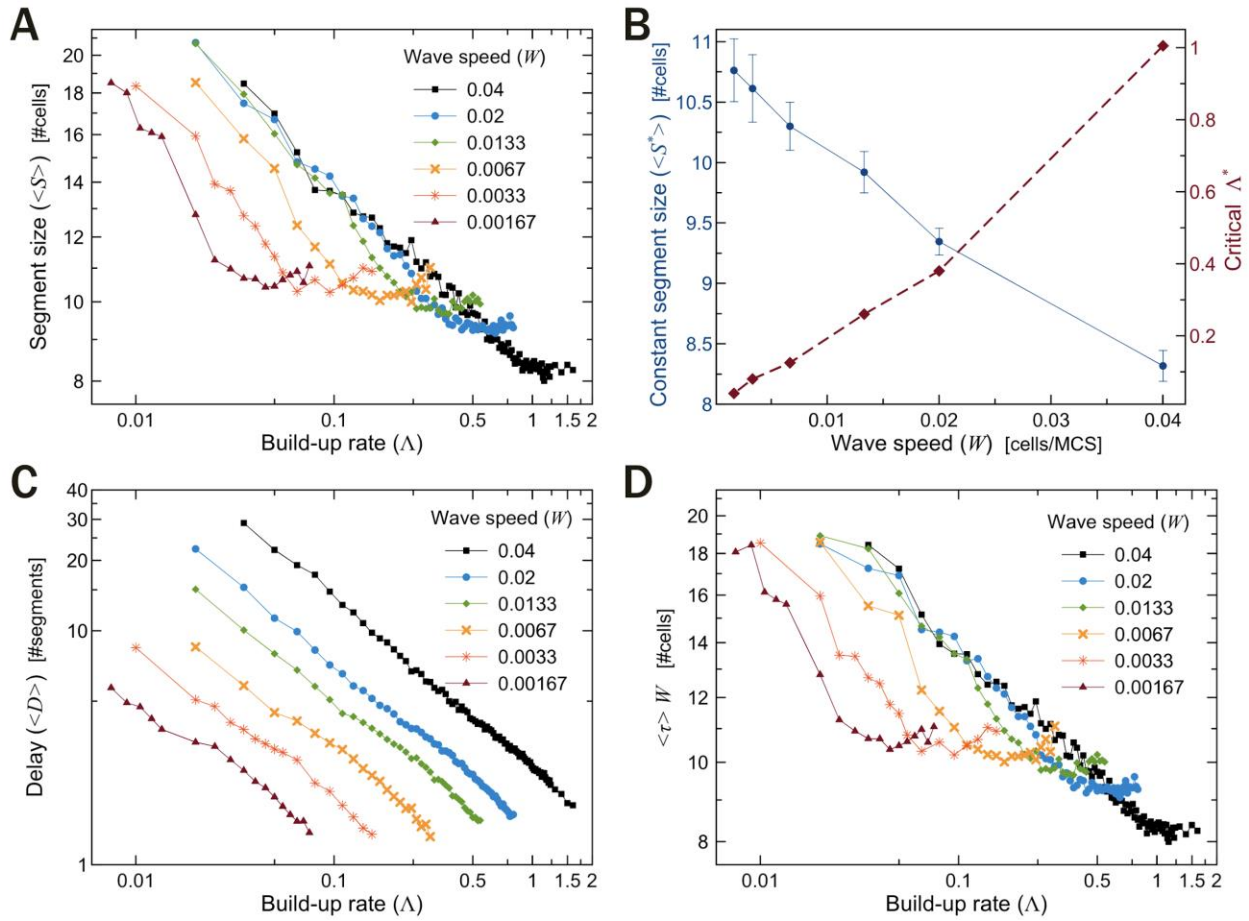

Figure 5 - Segmentation as a function of apical contractility build-up rate
(**A**) Average segment size $< S >$as a function of build-up rate of apical contractility Λ. Segment size decrease logarithmically with build-up rate, but stay constant for higher values of Λ. (**B**) Constant segment sizes $< S^* >$ (blue solid line) and critical build-up rates Λ^* (red dashed line) as functions of W. (**C**) Spatial delay between activation and boundary formation $< D >$ decreases linearly with Λ. (**D**) Average segmentation time $< \tau >$ as a function of Λ. Each individual curve has the same shape as the equivalent $< S >$ vs. Λcurves in (**A**). (**A**,**C**,**D**) Each line shows a qualitative similar behavior for different base values of the wave speed (W).

Next we fixed the wave speed $W$and varied the build-up rate of apical contractility Λ. Average segment sizes $< S >$ decrease logarithmically with higher build-up rates, but became constant after a critical value of Λ^* (Figure 5A,B). As before, segment sizes

outside the scaling regime ($< S^* >$) depends on the value of the wave speed W used in the simulations (Figure 5B). Again, these results can be understood in light of the way cell pair tension scales with segment size (Figure 2B). For slow build-up rates ($< \Lambda^*$), the sole factor determining segment size is the wave speed, with faster waves adding more cells to the forming segment before the boundary formation (Figure 4A). For higher build-up rates ($> \Lambda^*$), however, the rate of cell addition is not fast enough to overcome the increase in tension profile, which itself is a function of tissue size (Figure 2B).

The spatial delay between cell activation and boundary formation $< D >$ decreased linearly with the build-up rate, as expected: the faster the contractility build-up rate, the less time it takes for segments to form once all cells are actively constricting (Figure 5C). The average segmentation time $< \tau >$ had the same dependency on the build-up rate as the segment size $< S >$, as expected, given that $< S >= W < \tau >$ (Figure 5D).

Ratio of build-up rate to wave speed sets the transition of scaling regimes

The critical values of wave-speed $W^*$and build-up rate of apical contractility Λ^* for the transition between constant and segment size scaling regimes shown in Figures 4B and 5B are in fact related. Rescaling of the horizontal axis in Figures 4A and 5A for each curve by their corresponding values of Λ and W, respectively, shows that in both cases, the transition occurs around the same ratio of $\Lambda/W = 22\ MCS^2/cell$ (Figure 6A,B). This allows us to define a boundary transition in parameter space that separates regions

where segment sizes scales with variations in either Λ or W from regions where the segment sizes remain relatively constant with changes in one of these parameters (Figure 6C, green and blue regions). Note that we use the word *constant* in contrast to the size scaling of the segments with respect to either Λ or W, there is still a small and gradual change in segment sizes within the green region in Figure 6C (see Supplemental Figure 1).

The parameter space in Figure 6C also contains a grey region where the combinations of Λ and W leads to simulation artifacts. All data from this region were discarded in our analysis. The orange region and dashed boundary line will be defined momentarily.

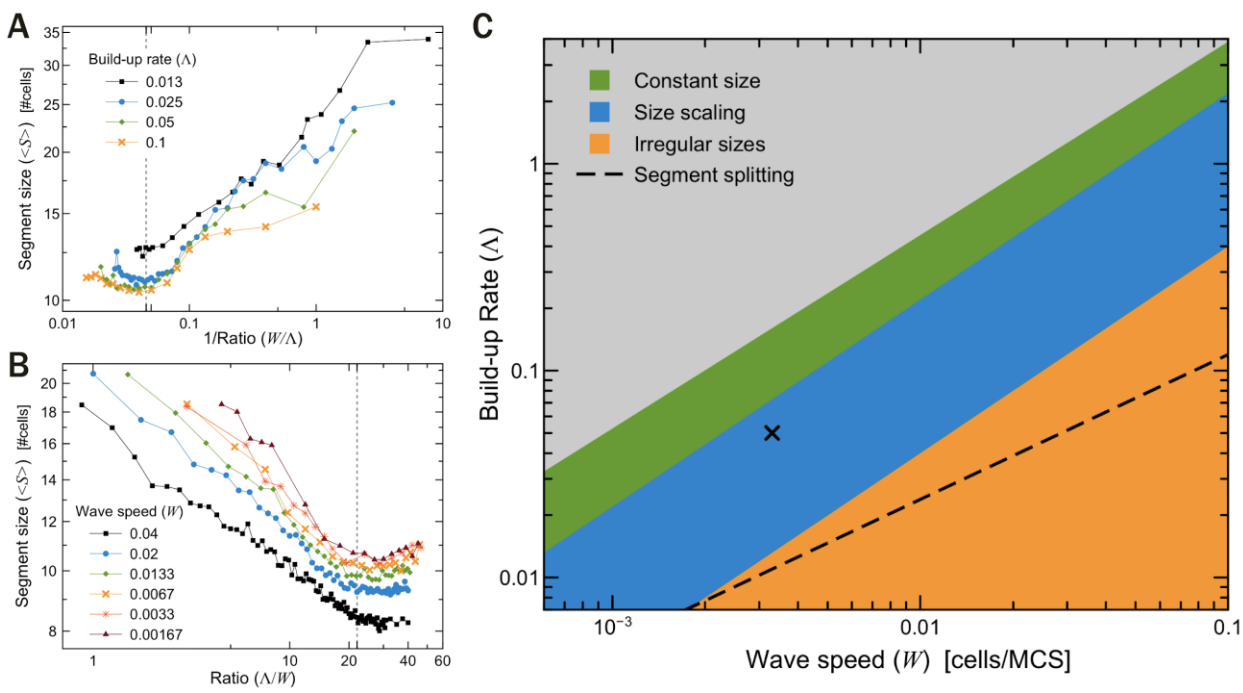

Figure 6 - Segmentation size scaling behavior
(**A**,**B**) Rescaled version of Figures 4A and 5B, showing average segment size $< S >$ as a function of (**A**) wave speed to build-up rate, and (**B**) its inverse. Vertical dashed line at $\Lambda/W = 22$ indicate transition threshold between constant size and scaling segment sizes. (**C**) Parameter space diagram showing regions where the combination of the parameters Λ and W leads to constant segment sizes (green),

scaling segment sizes (blue), or irregularly sized segments. Black dashed line show transitions from stable to splitting segments. Black X point indicates the reference simulation parameters (see Table 1). Grey region indicate parameters combinations that lead to simulation artifacts.

Segment sizes become irregular for low ratios of build-up rate to wave speed

While average segment size keeps scaling with higher wave speeds (W) or lower build-up rates of apical contractility (Λ), segment size distribution becomes irregular for higher ratios of Λ/W(Figure 7A-D). This can be visualized in plots of segment size variation, calculated as the ratio of standard deviation (σ) to the mean ($< S >$) (Figure 7E,F). This happens because when the wave speed is much faster than the build-up rate ($W \gg \Lambda$), a large group of cells starts to constrict at about the same time, the memory of the last cleft position is dissipated, and new clefts are more likely to appear anywhere in the tissue. We choose to classify segments as irregular when this variation is higher than 0.2. This corresponds, in our parameter space diagram, to a transition from regularly to irregularly sized segments at build-up to wave ratios of $\Lambda/W \sim 4$. Segmentation time variation ($\sigma/< \tau >$) is about 50% higher than size variation and had a similar dependence with Λ/W(see Supplemental Figure 2). This higher variation in segmentation time is expected from our mechanical model as the time of cleft formation is an emergent result rather than a direct input as in the clock and wavefront model.

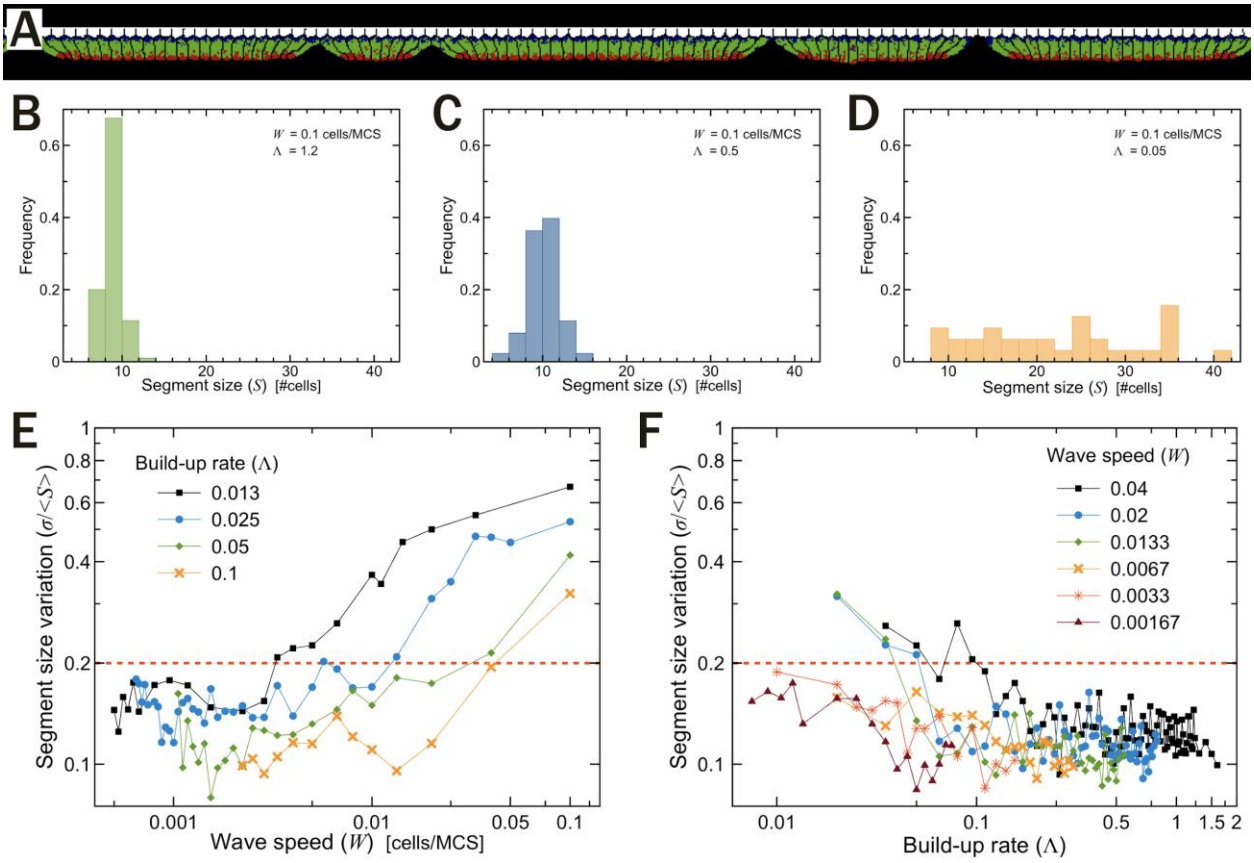

Figure 7 - Segment size variation
(**A**) Typical simulation output showing wide range of segment sizes from the irregular region (orange) of the parameter space in Figure 6C. (**B**-**D**) Histogram of segment size distributions for combinations of $\Lambda$and W in the constant size region (**B**), scaling region (**C**), and irregular region (**D**), of the parameter space over 5 trials. (**E**) Segment size variation (std/mean) as a function of build-up rate of apical cytoskeletal activity Λ. (**F**) Segment size variation as a function of wave speed W. (**E**,**F**) Dashed red lines at $\sigma/< S >= 0.2$ indicate threshold used to draw determine the region of irregular segment sizes in Figure 6C.

Apical constriction sets a higher limit on segment sizes

The above results show that initial segment sizes increase with faster wave speeds (Figure 4A) and slower build-up rates of apical contractility (Figure 5A). However, there

seems to be a higher limit on segment sizes. After their initial formation, larger segments are prone to split as the cells within them continue to increase their apical cytoskeletal activity strength (λ_A) and tension keeps building up until a new splitting event occurs near the middle of the formed segment (Figure 8A,B).

While the occurrence of a splitting event is proportional to the initial segment size (Figure 6C), the wave speed W has a more direct effect on the frequency of splitting, with higher build-up rates only delaying the appearance of splits (Figure 8D). Together these results suggest that our mechanical model of segmentation sets a higher limit on segment sizes depending on the speed of the wave with respect to the build-up rate of apical cytoskeletal activity (Figure 8C,D). Our results, however, did not point out to a specific ratio of Λ/W as predictive of a transition to a higher frequency (>0.1) of splitting events, but rather a nonlinear function $\Lambda = 0.6 * W^{0.7}$for the boundary between stable segments and splitting segments (dashed line in Figure 6C).

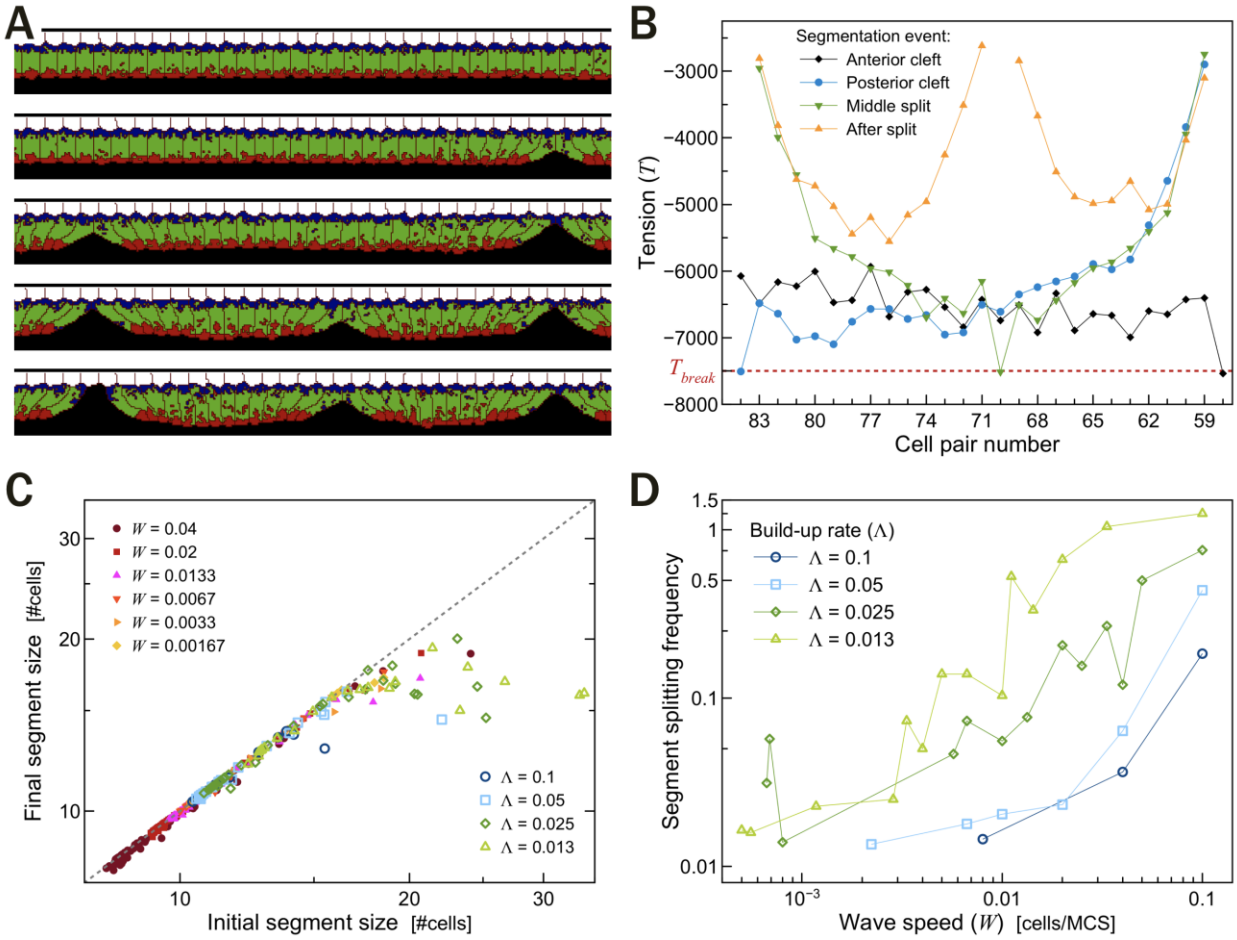

Figure 8 - Segment splitting
(**A**) Simulation snapshots showing the formation a splitting of a large segment (times, from top to bottom: 47000, 49000, 52000, 54000 and 56500 MCS). (**B**) Evolution of the tension profile for the splitting segment shown in (**A**). (**C**) Plot of average final versus initial segment sizes. Data points at the diagonal gray slashed lines indicate no splitting events. (**D**) Splitting frequency as a function of wave speed W.

Segment size as a function of maximum adhesion junction tension

So far, we had used a fixed apical to apical tension breaking threshold $T_{break} = -7500$. We now test the effects of varying the threshold at which tension causes the coupling

between neighboring cell's apical domains to break. At the extreme limit of $|T_{break}|$ near zero, the average segment size gets closer to 1 cell unit. Conversely, at high enough values, the tissue never segments and remains a single monolayer. As the magnitude of the breaking threshold increases between these ranges, the average segment sizes also increase, as expected (Figure 9A). Note however, that the splitting frequency is higher for low values of $|T_{break}|$, and zero for high values, with segments breaking in more than once for threshold values around $T_{break} = -2000$ (Figure 9B).

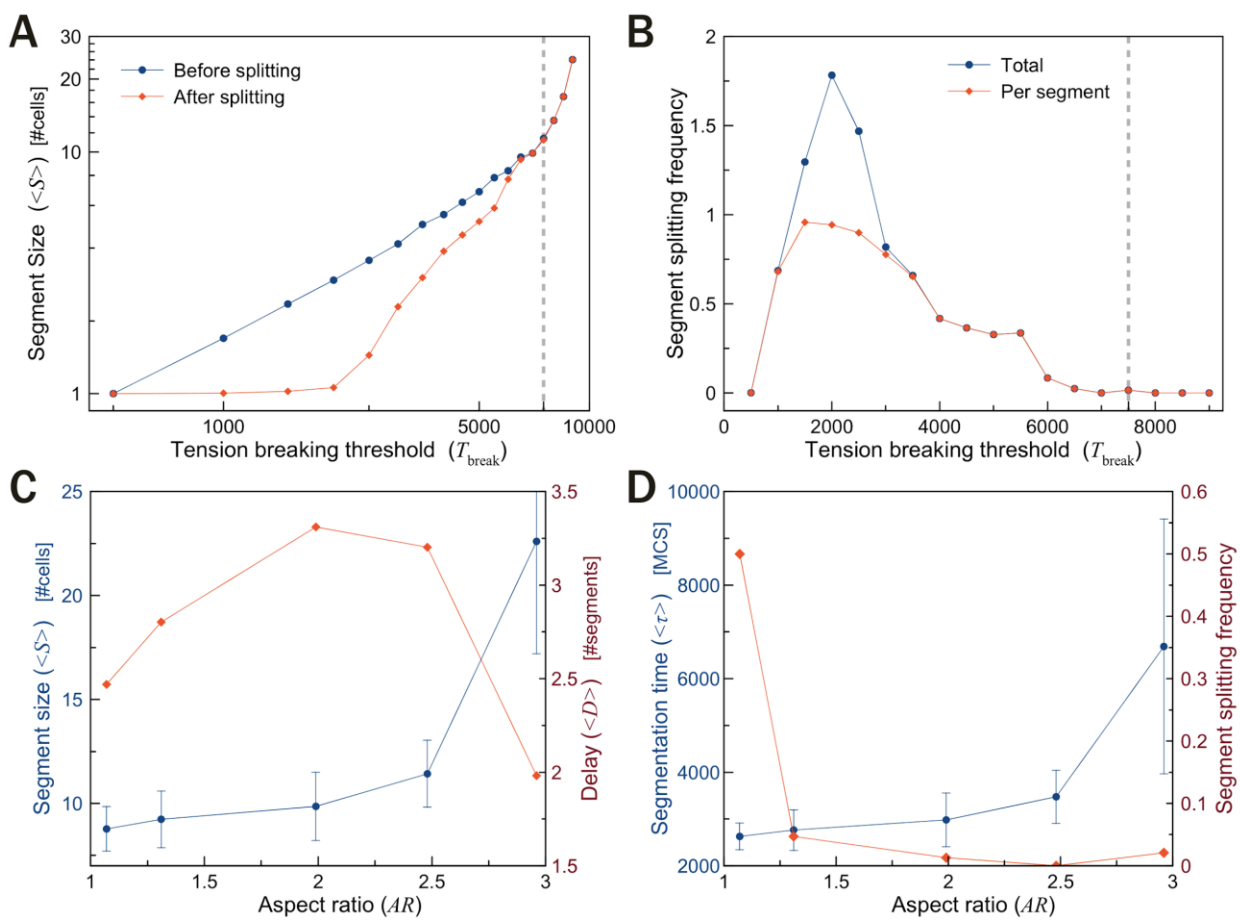

Figure 9 - Influence of junctional tension limit and cell shape on segmentation
(**A**) Average segmentation size $< S >$ as a function of the absolute value of tension breaking point $|T_{break}|$. Blue lines are initial segment sizes, red lines are segments sizes after splitting. (**B**) Average

number of splitting events per segment as a function of $|T_{break}|$. (**C**) Average segmentation size $< S >$ (blue) and spatial delay between activation and boundary formation $< D >$(red) as functions of cell aspect ratio AR. (**D**) Average segmentation time $< \tau >$ (blue) and frequency of segmentation splitting (red) as functions of cell aspect ratio AR.

Segmentation as a function of cell shape aspect ratio

In the somitic tissue, cells dynamically elongate while the process of boundary formation takes place. Since we have kept the length of the cell fixed for our simulations, we now evaluate how segment size depends on the aspect ratio of the cell ($AR = height/width$). Figure 9C shows the average segment size $< S >$ and delay $< D >$ as a function of cell aspect ratio. As expected, the more elongated they are the more cells can be packed into a segment. The delay, however, is a concave curve with respect to AR with a maximum around $AR = 2$. This can be understood as follows: the wider the cells ($AR < 2$) the harder it is to pack them into a segment made of wedge-shaped cells, so apical tension builds up quickly and clefts happen sooner, thus reducing both the segmentation time (blue line in Figure 9D) and the spatial delay between activation and boundary formation compared to the standard case (Figure 9C). Conversely, the more elongated cells ($AR > 2$), the greater the number of cells that can be packed into a segment and the longer it takes for consecutive boundaries to form. However, since the segments themselves are larger, the spatial delay, which is calculated in terms of segment sizes, also decreases. Figure 9D also shows that the segment splitting frequency (red line) is significantly higher for low aspect ratios, which can be understood as a result from the packing constraints that expedites the accumulation of tension

between apical cell pairs and make them more prone to splitting.

DISCUSSION

In this paper, we developed a mechanical model of tissue segmentation where a continuous wave of apical constriction activation coupled with maximum apical tension load set future somite boundaries. Our modeling effort is based on experimental observations of intensive cell rearrangements during somite formation (Martins et al. 2010) and our own SEM images (Figure 1A) that suggests that an early segmentation process is occuring at the dorsal side of the PSM about 4 somite lengths prior to the formation of the last somite. We interpreted the spatial segmentation of the dorsal epithelium into similarly sized cohorts of cells as the result of an increased longitudinal (dorsal-caudal) tension between the cells. A similar process is known to cause the appearance of periodic cracks on non-biological thin films subjected to tensile stress (Thouless (1990), Thouless et al (2011)). Here, however, our material is subdivided into discrete units; cannot be assumed as purely elastic; and the source of stress does not come from outside but is: i) generated internally by the cells, ii) is time-varying; and iii) is spatially inhomogeneous at any point of time. Given those differences we developed our own model of epithelial segmentation where we identified four key parameters: the speed of the wave (W), the rate of increase of apical contractility (Λ), the maximum apical cell-cell junction load (T_{break}), and the aspect ratio of the cells (AR) (Table 1).

While the parameters have been chosen to imitate segment size in chicken, we

comment that we need better tuning of the aspect ratio of the cells in the dorsal region. By the time the somites form, cells in this region can reach aspect ratios as high as 7. To compare results at these higher aspect ratios we would require re-parametrizing our cell volume to allow for sufficient apical surface so that the width is much greater than a chosen L_{AT}. While these changes are easily programmable, they come at a greater computational cost.

We found that our purely mechanical model is able to produce spatially and temporally regular segment sizes. Similar to the CW models, segment sizes scale (increases) with higher wave speeds. (Figure 4A). We found, however, that this scaling is not linear with wave speeds, as would be expected from a simple deterministic version of the CW model. There are two limits to this scaling behaviour, which can be characterised by Λ/Wratios alone (Figure 6C). An upper limit in segment sizes is reached for low ratios ($\Lambda/W < 4$), where initially formed segments are prone to splits due to mechanical instabilities; and a lower limit in the sizes is reached for high ratios ($\Lambda/W > 22$), where segment sizes do not scale with wave speeds. These limits in somite size are absent in CW models. Segmentation time in our model is not imposed but rather calculated as the difference in time for the appearance of the rostral and caudal boundaries. We find that it decreases with wave speeds and is insensitive to build-up rates (Figures 4D, 5D).

Ou model seems to have higher variations in the distribution of the segment sizes and formation time than existing mathematical implementations of the clock-and-wavefront model. In a real 3D scenario however, epithelialization along the dorsal sides does not

happen along a line as in our model, but within plane that also extends along the medial-lateral direction. Addition of these neighboring cells into our model would likely reduce variation in segment size and segmentation time. It is important to note that *in vivo* this early segmentation will be succeeded by epithelialization along other directions/planes reinforcing the initial boundaries and reducing the noise in the segment size distribution.

While our mechanical model drastically differs from the CW family of models with respect to the absence of a somitic intracellular clock, it still assumes the presence of some sort of caudally travelling wave, which does not need to be the same as the one postulated by the CW. We are agnostic about the nature of this wave, which can be either a cell-autonomous maturation process (starting from their addition to the tail-bud or a similar event), a tissue level processes, such as a read-out of FGF and RA levels, or a combination of both.

Finally, we are not proposing an alternative model for somitogenesis that replaces the proposed CW model, but rather exploring a complementary mechanism that is likely taking place in addition to an intra- and inter-cellular signalling mechanism. We found that our simple mechanical model of tissue segmentation is able to recapitulate most aspects of somitogenesis that a CW explain, such as the spatially and temporally periodic formation of somites and the correlation between somite size and wave-speeds as seen across species. In addition to that, our mechanical model also sets limits to the minimum and maximum sizes of somites and suggest an explanation for the observed

splitting of large somites formed in some perturbation experiments (*Stern & Bellairs (1984), Cooke (1978)*). As is often the case in biology, we speculate that the two processes are likely operating in conjunction to yield a robust morphological outcome. The combination of a mechanical and signalling process can explain, for example, the jumping of cells between forming somitic boundaries (*Kulesa et al (2002)*) where a cell mechanically constrained to be in one somite later moves and ingresses into the neighboring somite in as a response to its CW read-out.

Our current model, however, is to simple to explore such scenarios as it is restricted to a 1D view of the dorsal monolayer and is aimed to reproduce segmentation events prior to the formation of a full somite. Further developments of this basic model will include the self-organization of the PSM cells ventral to the dorsal monolayer and the expansion of the model to 3D. It is known that in chicken (*Martins et al (2010)*) different regions of the PSM epithelialize at different times, and it would be interesting to explore the implications of these observations in an augmented version of the mechanical model presented here.

REFERENCES

1. Pourquié, O. (2001). Vertebrate Somitogenesis. Annu Rev Cell Dev Biol, 17:311-50. https://doi.org/10.1146/annurev.cellbio.17.1.311
2. Christ, B., & Ordahl, C. P. (1995). Early stages of chick somite development. Anatomy and Embryology, 191(5), 381–396.

https://doi.org/10.1007/BF00304424

3. Cooke, J. (1975). Control of somite number during morphogenesis of a vertebrate, Xenopus laevis. Nature, 254(5497), 196–199. https://doi.org/10.1038/254196a0
4. Stern, C. D., Fraser, S. E., Keynes, R. J., & Primmett, D. R. N. (1988). A cell lineage analysis of segmentation in the chick embryo. Development, 104(SUPPL.), 231–244.
5. Primmett, D. R. N., Norris, W. E., Carlson, G. J., Keynes, R. J., & Stern, C. D. (1989). Periodic segmental anomalies induced by heat shock in the chick embryo are associated with the cell cycle. Development, 105(1), 119–130.
6. Meinhardt, H. Models of Biological Formation. 2nd ed. London: Academic Press; 1982.
7. Cotterell, J., Robert-Moreno, A., & Sharpe, J. (2015). A Local, Self-Organizing Reaction-Diffusion Model Can Explain Somite Patterning in Embryos. Cell Systems, 1(4), 257–269. https://doi.org/10.1016/j.cels.2015.10.002
8. Cooke, J., & Zeeman, E. C. (1976). A clock and wavefront model for control of the number of repeated structures during animal morphogenesis. Journal of Theoretical Biology, 58(2), 455–476. https://doi.org/10.1016/S0022-5193(76)80131-2
9. Palmeirim, I., Henrique, D., Ish-Horowicz, D., & Pourquié, O. (1997). Avian hairy gene expression identifies a molecular clock linked to vertebrate

segmentation and somitogenesis. Cell, 91(5), 639–648. https://doi.org/10.1016/S0092-8674(00)80451-1

10. Hester, S. D., Belmonte, J. M., Gens, J. S., Clendenon, S. G., & Glazier, J. A. (2011). A multi-cell, multi-scale model of vertebrate segmentation and somite formation. PLoS Computational Biology, 7(10). https://doi.org/10.1371/journal.pcbi.1002155

11. Tiedemann, H. B., Schneltzer, E., Zeiser, S., Hoesel, B., Beckers, J., Przemeck, G. K. H., & de Angelis, M. H. (2012). From dynamic expression patterns to boundary formation in the presomitic mesoderm. PLoS Computational Biology, 8(6). https://doi.org/10.1371/journal.pcbi.1002586

12. Baker, R. E., Schnell, S., & Maini, P. K. (2006). A clock and wavefront mechanism for somite formation. Developmental Biology, 293(1), 116–126. https://doi.org/10.1016/j.ydbio.2006.01.018

13. Dias, A. S., De Almeida, I., Belmonte, J. M., Glazier, J. A., & Stern, C. D. (2014). Somites without a clock. Science, 343(6172), 791–795. https://doi.org/10.1126/science.1247575

14. Nelemans, B. K. A., Schmitz, M., Tahir, H., Merks, R. M. H., & Smit, T. H. (2017). Mechanical stretching can modify the axial morphology of early chick embryos. https://doi.org/10.1101/211623

15. Martins, G. G., Rifes, P., Amaândio, R., Rodrigues, G., Palmeirim, I., & Thorsteinsdóttir, S. (2009). Dynamic 3D cell rearrangements guided by a fibronectin matrix underlie somitogenesis. PLoS ONE, 4(10). https://doi.org/10.1371/journal.pone.0007429

16. Duband, J. L., Dufour, S., Hatta, K., Takeichi, M., Edelman, G. M., & Thiery, J. P. (1987). Adhesion molecules during somitogenesis in the avian embryo. Journal of Cell Biology, 104(5), 1361–1374. https://doi.org/10.1083/jcb.104.5.1361
17. Bénazéraf, B., Francois, P., Baker, R. E., Denans, N., Little, C. D., & Pourquié, O. (2010). A random cell motility gradient downstream of FGF controls elongation of an amniote embryo. Nature, 466(7303), 248–252. https://doi.org/10.1038/nature09151
18. Mongera, A., Rowghanian, P., Gustafson, H. J., Shelton, E., Kealhofer, D. A., Carn, E. K., … Campàs, O. (2018). A fluid-to-solid jamming transition underlies vertebrate body axis elongation. Nature, 561(7723), 401–405. https://doi.org/10.1038/s41586-018-0479-2
19. Meier, S. (1979). Development of the chick embryo mesoblast: Formation of the embryonic axis and establishment of the metameric pattern. *Developmental Biology*, *73*(1), 25–45. https://doi.org/10.1016/0012-1606(79)90135-0
20. Tam, P. P. L., Meier, S., & Jacobson, A. G. (1982). Differentiation of the Metameric Pattern in the Embryonic Axis of the Mouse: II. Somitomeric Organization of the Presomitic Mesoderm. *Differentiation*, *21*(1–3), 109–122. https://doi.org/10.1111/j.1432-0436.1982.tb01203.x
21. Stern, C. D., & Piatkowska, A. M. (2015). Multiple roles of timing in somite formation. Seminars in Cell and Developmental Biology, 42, 134–139. https://doi.org/10.1016/j.semcdb.2015.06.002

22. Dubrulle, J., Mcgrew, M. J., & Pourquie, O. (2001). FGF signaling controls somite boundary position and Regulates Segmentation Clock Control of Spatiotemporal Hox Gene Activation. Cell, 106, 219–232.
23. Shirinifard, A., Glazier, J. A., Swat, M., Gens, J. S., Family, F., Jiang, Y., & Grossniklaus, H. E. (2012). Adhesion failures determine the pattern of choroidal neovascularization in the eye: A computer simulation study. PLoS Computational Biology, 8(5). https://doi.org/10.1371/journal.pcbi.1002440
24. Baker, P. C., & Schroeder, T. E. (1967). Cytoplasmic filaments and in the amphibian. Developmental Biology, 15, 432–450.
25. Pilot, F., & Lecuit, T. (2005). Compartmentalized morphogenesis in epithelia: From cell to tissue shape. Developmental Dynamics, 232(3), 685–694. https://doi.org/10.1002/dvdy.20334
26. Martin, A. C., & Goldstein, B. (2014). Apical constriction: Themes and variations on a cellular mechanism driving morphogenesis. Development (Cambridge), 141(10), 1987–1998. https://doi.org/10.1242/dev.102228
27. Sawyer, J. M., Harrell, J. R., Shemer, G., Sullivan-Brown, J., Roh-Johnson, M., & Goldstein, B. (2010). Apical constriction: A cell shape change that can drive morphogenesis. Developmental Biology, 341(1), 5–19. https://doi.org/10.1016/j.ydbio.2009.09.009
28. Pearl, E. J., Li, J., & Green, J. B. A. (2017). Cellular systems for epithelial invagination. Philosophical Transactions of the Royal Society B: Biological Sciences, 372(1720), 0–3. https://doi.org/10.1098/rstb.2015.0526

29. Martin, A. C., Gelbart, M., Fernandez-Gonzalez, R., Kaschube, M., & Wieschaus, E. F. (2010). Integration of contractile forces during tissue invagination. Journal of Cell Biology, 188(5), 735–749. https://doi.org/10.1083/jcb.200910099
30. Graner, F., & Glazier, J. A. (1992). Simulation of biological cell sorting using a two-dimensional extended Potts model. *Physical Review Letters*, *69*(13), 2013–2016. https://doi.org/10.1103/PhysRevLett.69.2013
31. Swat, M. H., Thomas, G. L., Belmonte, J. M., Shirinifard, A., Hmeljak, D., & Glazier, J. A. (2012). Multi-Scale Modeling of Tissues Using CompuCell3D. In Methods in Cell Biology (Vol. 110). https://doi.org/10.1016/B978-0-12-388403-9.00013-8
32. Belmonte, J. M., Clendenon, S. G., Oliveira, G. M., Swat, M. H., Greene, E. V., Jeyaraman, S., Bacallao, R. L. (2016). Virtual-Tissue computer simulations define the roles of cell adhesion and proliferation in the onset of kidney cystic disease. *Molecular Biology of the Cell*, *27*(22), 3673–3685. https://doi.org/10.1091/mbc.E16-01-0059
33. Rifes, P., Carvalho, L., Lopes, C., Andrade, R. P., Rodrigues, G., Palmeirim, I., & Thorsteinsdóttir, S. (2007). Redefining the role of ectoderm in somitogenesis: A player in the formation of the fibronectin matrix of presomitic mesoderm. *Development*, *134*(17), 3155–3165. https://doi.org/10.1242/dev.003665
34. Thouless, M.D. Crack Spacing in Brittle Films on Elastic Substrates. (1990) Journal of the American Ceramic Society. 73(7), 2144-46

35. Thouless, M. D., Li, Z., Douville, N. J., & Takayama, S. (2011). Periodic cracking of films supported on compliant substrates. *Journal of the Mechanics and Physics of Solids*, *59*(9), 1927–1937. https://doi.org/10.1016/j.jmps.2011.04.009
36. Stern, C. D., & Bellairs (1984). The roles of node regression and elongation of the area pellucida in the formation of somites in avian embryos. *Development*, 81, 75–92 https://doi.org/10.1126/science.1075544
37. Cooke, J. (1978). Somite abnormalities caused by short heat shocks to pre-neurula stages of Xenopus laevis. *Journal of Embryology and Experimental Morphology*, *VOL. 45*, 283–294.
38. Kulesa, P. M., & Fraser, S. E. (2002). Cell dynamics during somite boundary formation revealed by time-lapse analysis. *Science*, 298(5595), 991–995. https://doi.org/10.1126/science.1075544

ACKNOWLEDGMENTS

The authors would like to thank Dr. James P. Sluka for helpful discussions. This work was supported by NIH grants R01 GM076992, U01 GM111243 and R01 GM077138.